Instability mechanisms in meandering streamwise vortex pairs of upswept afterbody wakes

Rajesh Ranjan [a,b,*], J.-Ch. Robinet [c], Datta Gaitonde [a]

[a] Mechanical and Aerospace Engineering, The Ohio State University, Columbus, 43210, OH, USA
[b] Aerospace Engineering, IIT Kanpur, Kanpur, 208016, Uttar Pradesh, India
[c] DynFluid Lab., Arts & Métiers Paris - 151, Bd. de l'Hôpital, 75013, Paris, France

ARTICLE INFO

Keywords:
Vortical flows
Elliptic stability
Counter-rotating vortices
Cargo aircraft
Afterbody wakes

ABSTRACT

Wakes of upswept afterbodies are often characterized by counter-rotating streamwise vortex pairs which meander in space. One application concerns aft regions of cargo aircraft, which are characterized by a relatively flat upswept base. Here we consider a canonical configuration comprised of a cylinder with upswept basal surface. The resulting longitudinal vortices, which are much closer to each other than wing-tip vortices, can adversely influence paratrooper and cargo drop operations as well as trailing aircraft. The unsteady dynamics of these vortices are examined using spatio-temporally resolved Large-Eddy Simulations (LES) and stability considerations. Emphasis is placed on understanding the potential instability dynamics responsible for meandering, which was observed, characterized and quantified at a representative location downstream of the body. The dynamics is then successfully mapped to a matched Batchelor vortex pair, and spatial and temporal stability analyses are performed with both counter-rotating vortices in the computational domain. Both spatial and temporal analyses reveal dipole structures associated with $|m| = 1$ elliptic modes as dominant modes in afterbody vortices. A short-wave elliptic instability mode is found to dominate the meandering motion in the vortex pair; this mode was stable in the case of an isolated vortex. Further, the strain due to axial velocity plays a key role in the instability and therefore breakdown. The low frequency of the unstable mode (Strouhal number $St_D \simeq 0.3$ based on cylinder diameter) is consistent with the spectral analysis of meandering in the LES. Stability analyses at very low-wavenumber do not exhibit any unstable mode suggesting an absence of the Crow instability.

1. Introduction

Vortices associated with different flows such as those behind wingtips [1], delta-wings [2] and upswept afterbodies [3] display meandering or wandering motion. This phenomenon is usually characterized by the displacement of instantaneous vortex cores, whose centers display complex trajectories that can mask mean vortex characteristics. Understanding the dynamics of vortex meandering has been an interest to researchers for several decades. Some early efforts [4] ascribed meandering phenomena in wind tunnels to the disturbance environment *i.e.,* free-stream turbulence effects in the test environment. This attribution was motivated by the fact that some experiments on wingtip vortices [5] displayed coherent side-to-side motions, similar to those associated with wandering at zero angle of attack *i.e.,* when no coherent vortices are formed. Subsequently, experimental efforts [6,7] have observed that wandering amplitude increases with downstream distance, which is indicative of the possible existence of an instability mechanism.

Significant efforts towards understanding the mechanism have been made through the widely used linear stability approach, which discerns inherent instability mechanisms inside the vortex that may be responsible for the breakdown and therefore meandering. Many of these studies, only a few of which are cited here for brevity [8–11], seek to understand the meandering of wake vortices modeled on isolated constructs of vortex models, and as such, are representative of trailing edge or wingtip vortices. These are well separated, usually by the size of the wingspan. More recently, receptivity studies are also performed on these isolated vortex models [12], which provides further insights into the nature of external forcing responsible for meandering behavior. Therefore, the vorticity dynamics of an isolated vortex, especially those occurring at short wavelengths, can be a good representative of well-separated counter-rotating vortex pair.

Typically in these studies, a theoretical vortex model representative of a given flow vortex is considered [13] and instabilities associated with external strain and due to the presence

* Corresponding author at: Aerospace Engineering, IIT Kanpur, Kanpur, 208016, Uttar Pradesh, India.
E-mail address: rajeshr@iitk.ac.in (R. Ranjan).

of the surrounding wake are investigated. The Batchelor vortex model that includes the effects of axial velocity, for example, has been fruitfully employed in some recent studies. At high swirl and Reynolds numbers, Parras and Fernandez-Feria [14] connected the stability of these vortices to the dynamics of actual trailing vortices. Through rigorous spatial stability analysis, they showed that at very high Reynolds numbers, absolute instabilities are present only in the presence of an axial velocity. Edstrand et al. [9,15] used temporal and spatial stability analyses of a model Batchelor vortex resembling a tip vortex behind a NACA 0012 wing. A key finding was the presence of marginal elliptic stability [16] as a possible mechanism for meandering. This was also confirmed by Cheng et al. [17], who examined the problem at a range of Reynolds numbers and angles-of-attack in water tunnel experiments and performed corresponding linear stability analyses of a fitted Batchelor vortex model. Optimal perturbation analysis by Navrose et al. [18] for a trailing vortex system concluded that random perturbations near the wing surface, with relatively low initial energy, can non-linearly trigger vortex displacement.

The focus of the current work is on vortices that lie relatively close to each other. This arrangement results in strong vortex meandering effects but has received relatively less attention. Typical flows of interest are those on the base of upswept afterbodies [3], such as those found in military cargo aircraft [3,19], Ahmed body configuration [19], high-speed cars [20,21] and even trains [22]. On these configurations, a high upsweep angle ($15^\circ < \phi < 45^\circ$) causes flow separation near the turning of the elliptical base. The separated shear layer eventually develops into a counter-rotating vortex pair that meanders downstream of the body. The strengths of these vortices primarily depend on the upsweep angle. Since such counter-rotating vortex pairs are formed on the same basal surface, they are much closer to each other than trailing-edge vortices on aircraft wings. The streamwise velocity between the vortices may never reach the free-stream value while the downward induced velocity may be higher; this circumstance affects the different instability and breakdown mechanisms at play. For example, the temporal stability results of Hein and Theofilis [23], on a pair of Batchelor vortices exhibiting long-wavelength (Crow) instability, found stronger modification of the instability characteristics for the vortex pair system relative to the isolated vortex. Therefore, analyzing such systems requires consideration of both the vortices in the pair in the computational domain for stability analysis. In these cases, the resolution of both the vortices, as well as the wake region between, becomes imperative [23,24]. Further, the relatively innocuous farfield also needs proper treatment to avoid any boundary effects. This naturally increases the computational cost significantly compared to single vortex analysis [23,25], and therefore such studies are scarce in the literature.

The present work investigates such flows through an effective combination of high-fidelity computations, vortex characterization techniques as well as linear stability analysis. The specific configuration considered is inspired by the aft fuselage model of a typical cargo aircraft [3] as shown in Fig. 1. The full configuration consists of a nose section (spherical or ogive forebody) followed by a main cylindrical section of diameter D. The trailing end of the cylinder is cut by a slanted base, whose angle with the horizontal is ϕ, giving rise to upswept afterbody with an upstream apex (UA) and a downstream apex (DA) as the extreme endpoints on the base. The range of upsweep angles typically employed in military transport aircraft varies from $15^\circ \leq \phi \leq 28^\circ$; we select 20° as a representative value that generates the phenomena of interest.

The complexity of the surrogate cargo afterbody flow is associated with the presence of separation bubbles, rollup and flapping of the shear layer, vortex-shear layer interactions and vortex–vortex interactions as detailed in several experimental [3,27] and computational [28,29] studies. The proximity of the vortices results in significant vortex–vortex interactions and vortex meandering. Through PIV measurements in a water tunnel, Bulathsinghala et al. [3,30] observed the displacement of streamwise-oriented vortex cores, whose amplitude changes with downstream distance. Further, control efforts of these vortices through pulsed blowing exhibited an increase in meandering [31]. Zigunov et al. [27] observed low-frequency oscillations ($St_D \sim 0.4$, where St_D is the Strouhal number based on diameter) in their experiments and postulated this to be related to meandering due to interactions between the afterbody vortices in the pair. Garmann and Visbal [28] also found clear signs of meandering in their high fidelity simulations through unsteady vortex characterization. From a practical point of view, the presence of vortex meandering causes significant unsteadiness for long distances downstream, which is a major concern for designers. The unsteadiness and meandering motion can affect payload accuracy and paratrooper safety, as well as impose constraints on distance from trailing aircraft and airport operations [32].

Details of the counter-rotating vortex pair in the work have been obtained through validated LES of the afterbody configuration shown in Fig. 1. The meandering analysis is performed at a location sufficiently downstream of the base, where an unambiguous description of the mean vortex can be obtained without much interference of the shear layer. At this location, both vortices in the pair display meandering that is independent of shear-layer effects, and are matched to Batchelor vortices of suitable parameters, as discussed below. Finally, temporal and spatial stability analyses are performed on this vortex system and instability modes are analyzed. The instability mechanisms for isolated vortex and vortex pair systems are compared, as are the mechanisms with and without axial velocity that acts as a strain. Although detailed investigations pertain to a presence or absence short-wavelength (typically elliptic) instability, an attempt is made to study the long-wavelength Crow instability by varying the wavenumber.

2. Methodology

The configuration considered, shown earlier in Fig. 1 is a three-dimensional axisymmetric cylinder with a trailing sectional cut based on the upsweep angle $\phi = 20^\circ$. The chosen Reynolds number $Re_D = 2.5\times10^4$ is one of those based on the experimental campaign of Zigunov et al. [26]. Although this Re is low compared to actual flight conditions, several experimentalists [30,33,34] note that the primary features of the flow behind an afterbody at a given upsweep angle of the base are largely independent of Re. The high-fidelity simulations of Ranjan et al. [29], which form the basis of the present work and are summarized for brevity below, have independently confirmed this observation.

As shown in Fig. 1, x, y, z denote streamwise, vertical and spanwise directions respectively in the chosen coordinate system. All geometrical parameters are non-dimensionalized based on cylinder diameter (D) and free-stream velocity U_∞. Axial distances are designated in terms of $L = D\cot(\phi)$, the distance between the upstream and downstream apexes, which are marked in Fig. 1. The vertical plane at $z = 0$ will be referred to as a mid-plane or symmetry plane.

2.1. Large Eddy simulation

The compressible Navier–Stokes equations are solved in a curvilinear (ξ, η, ζ)-coordinate system:

$$\frac{\partial}{\partial\tau}\left(\frac{Q}{J}\right) = -\left[\left(\frac{\partial F_i}{\partial\xi}+\frac{\partial G_i}{\partial\eta}+\frac{\partial H_i}{\partial\zeta}\right)+\frac{1}{Re}\left(\frac{\partial F_v}{\partial\xi}+\frac{\partial G_v}{\partial\eta}+\frac{\partial H_v}{\partial\zeta}\right)\right] \quad (1)$$

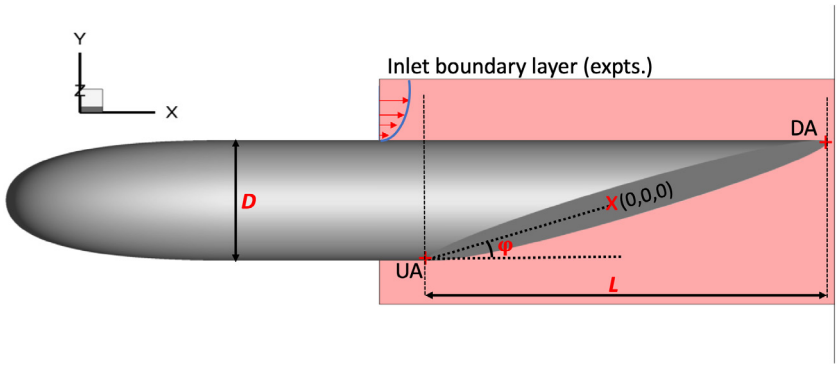

Fig. 1. Canonical configuration employed to reproduce the streamwise-oriented wake vortex pair. Cylinder diameter is D and upsweep angle is $\phi = 20°$. The coordinate axis origin is located at the center of the upswept surface, (0, 0, 0), (red cross: ×) and the axial slant length is $L = D\cot(\phi)$. The shaded colored region encompasses the near-computational domain. The upstream apex (UA) and the downstream apex (DA) are located at $x/D = -\cot(\phi)/2, y/D = -0.5, z/D = 0$ and $x/D = \cot(\phi)/2, y/D = 0.5, z/D = 0$ respectively. To describe the flow around the upswept base, the transformation $X = x + D\cot(\phi)/2$ is used such that UA and DA are at $X/L = 0$ and $X/L = 1$ respectively. At the inlet, simulated boundary layer data matching the experiments [26] are used. (For interpretation of the references to color in this figure legend, the reader is referred to the web version of this article.)

where, $Q = [\rho, \rho u, \rho v, \rho w, \rho E]^T$ denotes the solution vector, defined in terms of the fluid density ρ, Cartesian velocity components (u, v, w) and total specific energy $E = T/(\gamma - 1)M^2 + (u^2 + v^2 + w^2)/2$. Here, M is the Mach number of the flow, which is set to 0.1. γ is the ratio of the specific heats and T is the fluid temperature. $J = \partial(\xi, \eta, \zeta, \tau)/\partial(x, y, z, t)$ denotes the Jacobian of the transformation from Cartesian (x, y, z) to curvilinear (ξ, η, ζ)-coordinate system. The above governing equations are complemented by the ideal gas law, written in non-dimensional variables as $p = \rho T/\gamma M^2$. Sutherland's law is used to express fluid dynamic viscosity μ as a function of temperature T.

The computational domain, as well as grid topology employed, are shown in Fig. 2. The nose section of the body, shown in Fig. 1, is not simulated; instead, the inflow to the domain is placed upstream of the base at a location where experimental profiles are available. At this location, results from precursor simulations are performed on an axisymmetric body to match the experimental conditions used in [26]. Although no significant unsteadiness is noted in the profiles at the Reynolds number considered, the boundary layer may be susceptible to instabilities. Viscous no-slip and zero normal pressure gradient boundary conditions are used on the cylinder surface, whereas freestream conditions were applied at the radial farfield boundary which is placed approximately 14D away from all surfaces. At the downstream farfield boundary, Neumann boundary condition with zero-gradient is specified for all flow variables.

A structured cylindrical grid is considered with a total of 485, 418 and 285 points in the longitudinal, radial and azimuthal directions respectively. The local mesh density is comparable to that employed by Garmann and Visbal [28] for a much higher Reynolds number. A p-refinement study using fourth- and sixth-order compact difference schemes with sixth-order and eighth-order implicit filters, demonstrates mesh independence as discussed in [29]. The filter serves both to ensure numerical stability, as well as to provide an implicit subgrid closure mechanism [35]. Time-stepping is performed using the implicit Beam-Warming scheme [36] with the diagonalization of Pulliam and Chaussee [37]. The simulations are performed with a constant non-dimensional time-step of $\Delta t = 2.5\times10^{-4}$, which is sufficient to ensure temporal accuracy. Further details of the numerical algorithm used for the simulations can be found in [38,39].

2.2. Linear stability approach

Classical linear stability approach has been used for the current vortex pair analysis as briefly delineated below. Results are presented with the incompressible formulation since, as shown below, the compressible formulation yields essentially the same results. The incompressible Navier–Stokes equations in non-dimensional form are given by:

$$\nabla.\boldsymbol{u} = 0 \tag{2a}$$

$$\frac{\partial \boldsymbol{u}}{\partial t} + (\boldsymbol{u}.\nabla)\boldsymbol{u} = \nabla p + Re^{-1}\nabla^2\boldsymbol{u} \tag{2b}$$

where $\boldsymbol{u} = \{u, v, w\}^T$. The flow field is decomposed into a basic state $(\bar{\boldsymbol{u}}, \bar{p})$ and perturbations $(\boldsymbol{u}', p')$, with the former satisfying Eqs. (2). The equations governing linear perturbations are then:

$$\nabla.\boldsymbol{u}' = 0 \tag{3a}$$

$$\frac{\partial \boldsymbol{u}'}{\partial t} + (\boldsymbol{u}'.\nabla)\bar{\boldsymbol{u}} + (\bar{\boldsymbol{u}}.\nabla)\boldsymbol{u}' = \nabla p' + Re^{-1}\nabla^2\boldsymbol{u}' \tag{3b}$$

where the small non-linear terms, $(\boldsymbol{u}'.\nabla)\boldsymbol{u}'$, are ignored. For stability analysis, a modal form of the perturbations is assumed, with homogeneity in the x-direction

$$\{u', v', w', p'\}(x, y, z, t) = \{\tilde{u}, \tilde{v}, \tilde{w}, \tilde{p}\}(y, z)e^{i(kx-\omega t)} \tag{4}$$

where the quantities with $(\tilde{\bullet})$ are two-dimensional amplitude functions. Substituting this in the perturbation equations (3), the stability equations are obtained and different eigenvalue problems are formulated for temporal and spatial analyses as given in Appendix.

The eigenvalue problems are solved using the iterative Arnoldi [40] algorithm. Further, the shift-and-invert approach [41] in the Arnoldi algorithm is used to obtain faster convergence to desired eigenvalues. A large Krylov dimension ($k = 100$) is chosen to ensure that the relevant unstable eigenspectrum around the shift value is captured. For both temporal and spatial analysis, distant farfield boundaries are used to allow for homogeneous Dirichlet boundary conditions for all perturbation variables except for pressure, for which the Neumann boundary condition is appropriate.

For isolated vortex, a computational domain, whose size scales as $y_\infty/\delta \approx 20$, $z_\infty/\delta \approx 20$, where δ is the vortex core radius, is employed for the analyses. The domain used for the two vortex system is $y/\delta \in [-20;\ 20], z/\delta \in [-20 - b/2;\ 20 + b/2]$, where b is the separation between vortices. For discretization, we follow the approach suggested by Hein and Theofilis [23], where a mapping ζ_j of Chebyshev collocation points $\eta_j \in [-1;\ 1]$ is used, such that:

$$\zeta_j = \zeta_\infty \frac{\tan\frac{c\pi}{2}\eta_j}{\tan\frac{c\pi}{2}} \tag{5}$$

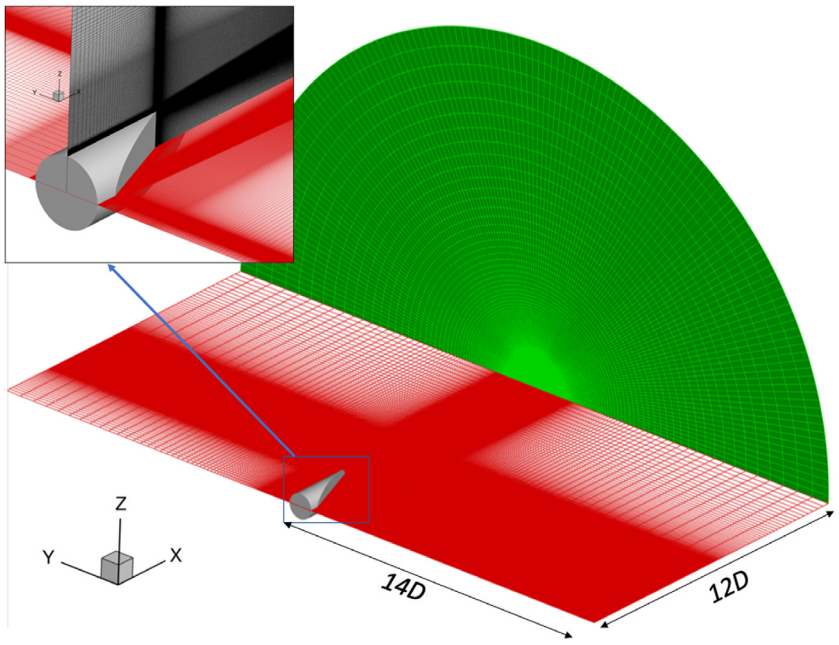

Fig. 2. Computational domain and grid employed for current afterbody simulations. Grids on the center *xy*-plane of the base, and at downstream farfield location are shown to illustrate the grid topology. Cylindrical grid with origin at the center of the base and periodicity in the azimuthal direction is used. Domain extends 12*D* and 14*D* in downstream (green) and radial farfield (red) directions respectively. Bottom half of the computational domain is not shown. (For interpretation of the references to color in this figure legend, the reader is referred to the web version of this article.)

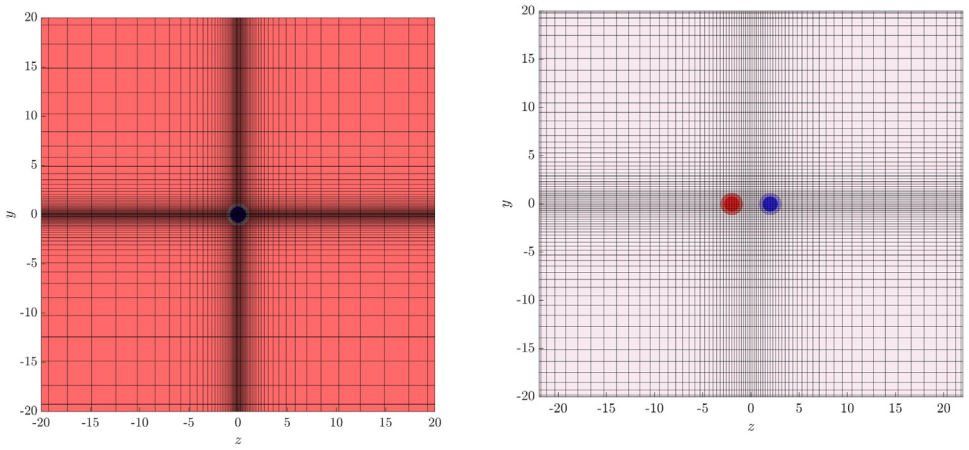

(a) Isolated vortex $(72 \times 72, c = 0.975)$. (b) Vortex pair $(100 \times 100, c = 0.75)$.

Fig. 3. Spatial discretization for stability analysis.

where ζ_∞ is the farfield boundary. The stretching parameter $c \in (0,\ 1]$ defines the clustering of grid points near the vortex core. Higher c provides more clustering near the vortex core while imposing a relatively coarser grid away from the core. This distribution of points will be referred to as the Cheb-tanh grid.

Fig. 3(a) shows a typical grid clustering for $N_y = N_z = 72$, $c = 0.975$, ensuring that the vortex at the center is adequately resolved. For a vortex pair, the grid distribution requires further consideration than for a single vortex, because of their separation along the z-axis connecting their centers. For this, the stretching parameter, c, is relaxed to encompass both the vortices and the region between them as shown in Fig. 3(b).

Table 1 shows validations for both temporal and spatial stability codes used in the study. For the temporal approach, the classical q-vortex at $q = 0.475$, $Re = 100$, $k = 0.418$ is chosen; this problem was first examined by Mayer and Powell [43] and subsequently used for validation in several studies [15,23,25]. The results for the unstable mode are reported along with the reference results from [25]. Excellent convergence is obtained with the mapped Cheb-tanh discretization, even for a slightly smaller domain in $[-15\ 15]$ and moderate grid size. The stretching parameter in this discretization is fixed at $c = 0.975$, ensuring that the vortex at the center is adequately resolved. A good match is also obtained with the sixth-order finite difference (FD6) approach albeit at a higher resolution. The table also includes a result when a fully compressible stability solver (FD6(C)) is used for the same q-vortex analysis at a low Mach number ($M = 0.1$). Comparing the results between incompressible and compressible solvers with similar grid and numerical schemes, we note only a minor difference of about 1% in the frequency and 0.44% in the growth rate.

For the spatial code validation, the Batchelor vortex study by Paredes [42] at $\kappa = 0.8$, $\gamma = 0.8$, $\delta = 1$, $Re = 3000$ is used for reference. In Table 1, results for $m = 1$, $\omega = 0.86$) are compared

Table 1
Validation of stability analyses techniques for q-vortex (temporal) and Batchelor vortex (spatial) test cases. The leading eigenvalues in both analyses are close to those in the reference literature. Effects of domain sizes and different difference schemes are minor. Temporal analysis is also performed with a compressible solver with sixth-order finite-difference scheme (FD6(C)). At low Mach number ($M = 0.1$), compressible solver yields leading modes close to those obtained with fully incompressible code.

Domain	Scheme	Resolution	λ_1
Temporal: q-vortex, $q = 0.475$, $Re = 100$ **Ref.** Paredes et al. [25]: $\lambda_1(k_r = 0.418) \equiv \omega_r + \omega_i i = 0.02835 + 0.00962i$			
$[-15\ 15]$	Cheb-tanh	40×40	$0.02834 + 0.00961i$
$[-20\ 20]$	Cheb-tanh	60×60	$0.02833 + 0.00960i$
$[-15\ 15]$	FD6	101×101	$0.02853 + 0.00998i$
$[-15\ 15]$	**FD6(C)**	101×101	$0.02823 + 0.01002i$
Spatial: Batchelor vortex, $\kappa = 0.8$, $\gamma = 0.8, \delta = 1$, $Re = 3000$ **Ref.** Paredes [42]: $\lambda_1(\omega_r = 0.86) \equiv k_r + k_i i = 0.543 - 0.185i$			
$[-15\ 15]$	Cheb-tanh	40×40	$0.5534 - 0.184i$
$[-20\ 20]$	Cheb-tanh	60×60	$0.5490 - 0.180i$

against the values reported in [42]. Even with a moderate 40×40 grid, the frequency obtained in the current study is within 2% of the reported value; the comparison improves with increase in grid size. For all the results in current afterbody vortices, Cheb-tanh grid is employed.

3. LES flowfield description

3.1. Three-dimensional flowfield

The overall features of the flow have been described in numerous works; only those aspects pertinent to the current stability analysis are represented here. Three-dimensional flowfield visualizations from the current Large Eddy Simulations (LES) are shown in Fig. 4. The dominant feature arising from flow separation around the periphery of the base region is a streamwise-oriented vortex pair downstream [3,26,28,29]. In Fig. 4(a), a Q-criterion [44] iso-level ($Q = 30$) is depicted, colored by streamwise vorticity, ω_x, together with select superposed streamlines to provide an indication of the swirling motion in the instantaneous flow. The counter-rotating streamwise vortex pair as well as the twisting motion of each vortex in the pair, are clearly evident. The turbulent flowfield arises as a result of the strong interaction between the separating shear layer and vortices in the region adjacent to the upswept base.

Fig. 4(b) displays the mean flowfield using the same flow variables. The mean was obtained by computing the time average over 700,000 snapshots encompassing the total non-dimensional time of $T_c \equiv tU_\infty/D = 175$. In the mean sense, each vortex in the pair gradually assumes an axisymmetric form in the region outside of the immediate vicinity of the upstream apex. Looking downstream, the left and right vortices have dominantly positive and negative streamwise vorticity components respectively. In the instantaneous flow, Fig. 4(a), there are smaller convecting structures that are washed out in the time-averaged sense. Depending on the Reynolds number, this structure persists in a range of $\phi \leq 45°$; descriptions at other upsweep angles in $24° \leq \phi \leq 45°$ may be found in [3,26] and [29]. At even higher upsweep angles ($\phi > 45°$) however, the flow changes to a turbulent wake regime typical of bluff-body wakes [19,29]. Hysteresis or bi-stable states are possible, typically at higher angles than that considered here [19,26,45] but these phenomena are outside the scope of the current effort.

The phenomenology of the formation of the vortical structures along the base may be summarized as follows. The boundary layer approaching the edge separates around the entire periphery to form a shear layer. The segment separating near the upstream apex rolls up to form a bubble structure in the symmetry plane (shown in the inset of Fig. 4(b)). The flow separating around the periphery is entrained into each vortical structure. The continuity of the vortex on the symmetry plane permits an alternative description of the vortex pair as leg components of a single horseshoe-like vortical structure. Each vortex leg then lifts away from the upswept base, at about the midway point to form the streamwise oriented pair. After the vortices orient away from the surface, the free shear layer arising from separation at the downstream apex continues to entrain fluid into the vortices for some distance behind the body. This interaction, although not crucial in the formation phase of the vortices, affects the motion downstream.

3.2. Streamwise vortices and meandering

Now, we discuss the evolution of streamwise vortices along the base and in downstream of the body. This is important as these vortices exhibit meandering [46] on respective crossflow planes, which may be related to their inherent stabilities. Fig. 5 shows the evolution of these vortices at various crossflow sections on the mean three-dimensional vortex field. These three-dimensional structures are obtained using the Q-criterion as before and shows the development along the base and further downstream in both vertical and spanwise directions. Along the vertical direction (xy-plane), the vortices originate at the upstream apex and detach at about $X/L = 0.5$, as discussed earlier. Vortices continue to evolve after this point with an inclination of about 5° from the streamwise axis. Looking the vortices in the xz-plane, we note the maximum separation of vortices at $X/L = 0.5$, after which the vortices come slightly closer to each other before becoming almost straight.

The 2D streamwise vortices at different crossflow planes ($X/L = 0.6, 1.0, 1.4, 1.8$) are shown through instantaneous ω_z contours. The vorticity fields show distortions in the cores as well as intense interactions of vortices with surrounding shear layers. At $X/L = 0.6$, the contorted cores appear very different from the mean vortices which are circular as evident from three-dimensional structure. These vortices also interact with the base shear layer and appear to be connected to base. At $X/L = 1.0$ and beyond, the instantaneous vortices continue to be distorted in shape, although there are also significant interactions with the shear layer coming from the top of the body, which diminishes with distance. Fig. 6 shows the mean vortex at a further downstream location, $X/L = 2.0$, along with a representative instantaneous picture. The mean flow is highly symmetric compared to distorted instantaneous flow. Similar to the results shown in [29], albeit for a higher upsweep angle, the mean circulations of left and right vortices here are exactly equal and opposite.

The distortions in vortex cores manifest as meandering when observed in time as the vortex centers present a complicated trajectory. These motions are highly intriguing and have been studied using stability analysis for several flows like wingtip vortices [9,47], where the counter-rotating vortices in the pair are far from each other. However, as shown in Fig. 5, in upswept afterbody flows, both the vortices form on the same basal plane and hence may have a greater influence on one another affecting the stability mechanism. In the later sections, we will investigate this by considering a suitable vortex pair as obtained from LES.

As the primary interest is in the inherent instabilities in the vortex pair, we isolate the effects of base or top shear layer by considering a vortex pair sufficiently downstream from the body. In this context, we discuss the detailed motion of each vortex at $X/L = 2.0$, where the immediate effects of the base

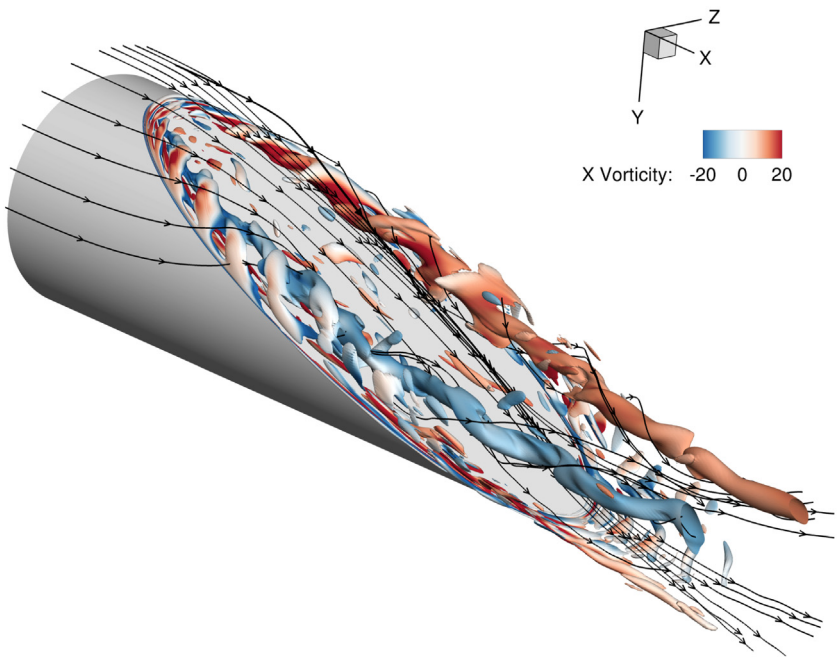

(a) Instantaneous flow

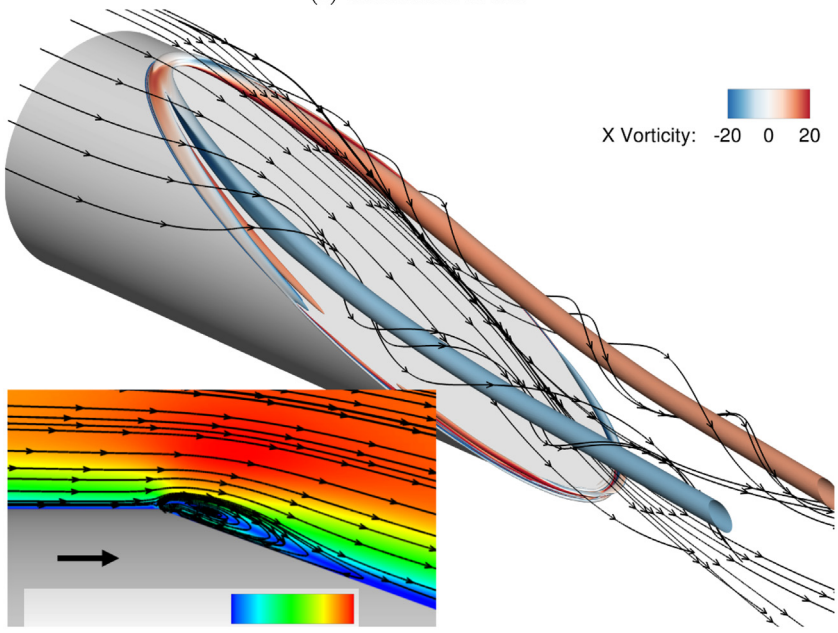

(b) Mean flow

Fig. 4. Longitudinal vortices behind the slanted body. An iso-surface of $Q = 30$ is plotted, colored by streamwise vorticity ω_x. The mean separation bubble near the upstream apex is shown in inset (b). The configuration is inverted with positive y-axis pointing downward for display purposes. (For interpretation of the references to color in this figure legend, the reader is referred to the web version of this article.)

region are expected to be greatly diminished. The circulation of the mean vortex does not change very much beyond $X/L = 1.2$ [29]. Further, the intervortical separations between the two vortices also remain nearly constant in this region (see Fig. 5). It is therefore expected that the characteristics of vortex pairs would not vary significantly behind the afterbody and therefore the vortex pair at $X/L = 2.0$ well represents the vortex system in afterbody flows at the upsweep angle of $\phi = 20°$. However, both the vortex strength as well as intervortical separation depend significantly on the upsweep angle [29], and therefore current observations do not directly translate to afterbody flows at other upsweeps.

Fig. 6(a) and (b) show the mean and instantaneous vortices at the location $X/L = 2.0$. Compared to mean vortices, the instantaneous vortices are elliptic. Further, a close examination of the vortices reveals the opposite sense of rotation of the fluctuations based on the sign of the mean vortex. The vortex cores for these vortices are identified using the Γ_1 approach [48]. The core radius for both the mean vortices in the pair is $\delta/D \simeq 0.0972$, while the separation between the two vortices is $b/D \simeq 0.5456$. This gives the ratio of radius to intervortical separation $\delta/b \simeq 0.1781$. This is an important parameter that determines the potential nature of instability and will be further discussed. For future reference, the two vortices in the pair are designated as **L** and **R** vortex based

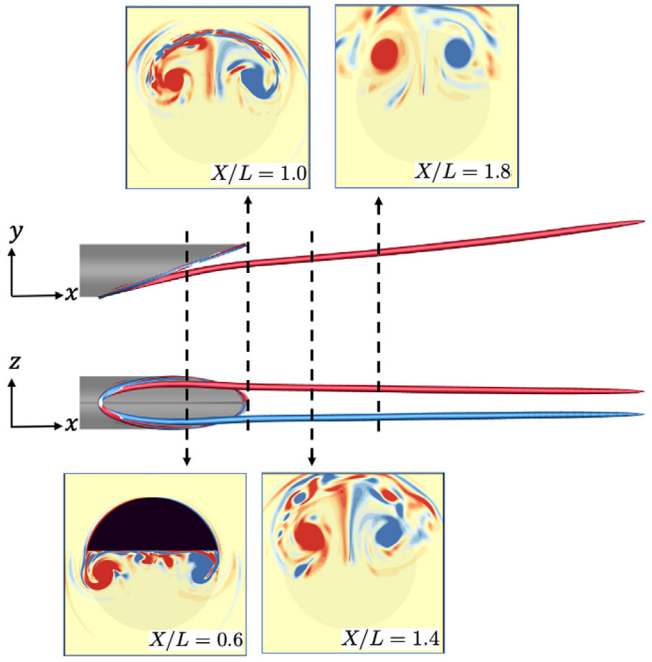

Fig. 5. Evolution of streamwise vortex along the base of the upswept surface. Fully 3D vortices are shown using the Q-criterion on the mean flow. Representative instantaneous 2D vortices are shown at $X/L = 0.6$, 1.0, 1.4 and 1.8 using non-dimensional ω_z contours between −5 and 5. Blue and red contour colors represent negative and positive vorticity fields respectively. (For interpretation of the references to color in this figure legend, the reader is referred to the web version of this article.)

on whether, looking downstream, they are located to the left or right of the symmetry plane respectively.

In order to show the complex meandering path of vortices at this location, we plot the displacement in the mean core with time as suggested by Green and Acosta [49]. The locus of vortex cores is presented in the form of a phase portrait in Fig. 7. The trajectory of each core using 100 snapshots, separated by a non-dimensional time $\Delta t = 0.025$, is shown on the crossflow (yz) plane. The initial and final positions of each core are marked with black and red circles, and the position of the mean vortex core is shown as a large magenta square. While the core of the **L**-vortex meanders in the clockwise direction, the meandering trajectory of the **R**-vortex is counter-clockwise. The sense of rotation is the same as the swirl of the vortex, similar to observations on delta wings [50]. The instantaneous location of each vortex core deviates significantly from the mean, with $\Delta d_{max}/D = 0.05$, where Δd_{max} is the maximum displacement of instantaneous core location from the mean. In order to quantify this phenomenon, the meandering amplitude a_m, defined as the average of distance between instantaneous core (z_i, y_i) and mean core locations (z_c, y_c), is measured:

$$a_m = \sqrt{\frac{1}{N}\sum_{i=1}^{N}\left[(z_i - z_c)^2 + (y_i - y_c)^2\right]} \tag{6}$$

a_m values are 0.0288 and 0.0282 for **L** and **R** vortex, respectively. Similar values of the amplitude for both the vortices indicate their statistically analogous behavior despite seemingly random motion.

In order to estimate the correlation between meandering in the two vortices, we compute the correlation coefficient, R, between **L** and **R** vortex by using the displacements of instantaneous cores from their respective mean positions. Smaller values of this coefficient indicate lower influence of the vortices on one another. The correlation coefficient thus obtained by considering 3,000 instantaneous vortices is $R = 0.1622$. This value is very near to that reported by Jackson et al. [51], but slightly higher than that of Bulathsinghala et al. [3]. According to Jackson et al. [51], these observations are rather independent of the streamwise location. To further probe the nature of the correlation, the Gaussian joint probability distribution function (JPDF) is plotted in Fig. 8(a). The maximum probability of the interaction between the two vortices is observed at $d_L/D = d_R/D \simeq 0.028$. Since the mean vortices are separated by $b/D \simeq 0.06$, a reasonable inference is that the interaction may only become important when the instantaneous vortices are closest to the symmetry plane. The JPDF diminishes as the vortices move away from the symmetry plane. Although the above analysis suggests the effects of vortices on one another are weak, these calculations do not include the crucial axial velocity component that can play a significant role in determining the instability mechanism responsible for the meandering of these vortices as discussed in Section 4.

The frequency of the meandering motion at this location is characterized using the spectral signature of the instantaneous vortices at the mean vortex core location. Fig. 8(b) shows the power spectral density (PSD) of fluctuations of v-velocity for the **R**-vortex using a long time-series signal, $tU_\infty/D > 60$. The signal shows a frequency band in Strouhal number based on diameter $St_D \equiv fD/U_\infty \in [0.3\ 2.0]$, with several low ($St_D \simeq 0.3, 0.6$) and high ($St_D \simeq 1.0, 1.4, 1.6$) frequency peaks. The maximum spectral energy is observed at $St_D \simeq 1.0$. Though not shown for brevity, similar frequency content is also obtained for the **L**-vortex. High-frequency peaks in the range $St_D \in [1.4\ 1.6]$ were also observed in the LES studies at high Reynolds number [28], whereas [27] reported strong tones at low-frequency, $St_D \simeq 0.4$, in addition to the high-frequency peaks for a range of Reynolds numbers. Zigunov et al. [27] also postulated the high-frequency content to be related to the shear layer downstream of the body, while the low-frequency fluctuations were conjectured to be related to interactions between the cores as observed in several vortex meandering studies [1,6,9]. Detailed stability analyses of the vortex pair are performed in the next section to investigate the vortex–vortex interactions as well as effects of the axial velocity component.

4. Linear stability analysis

Linear stability analysis is now employed to provide insights into the physical mechanism of meandering by extracting the underlying modal structures, frequencies and wavenumbers that form the basis for the observed phenomena. Jacquin et al. [52] have observed that the cooperative interactions between the vortices affect the similar frequency range as meandering. Two typical instabilities of interest due to the mutual induction between counter-rotating vortex pairs are those designated elliptic and Crow. The former is of short-wavelength and incurs an internal deformation of the vortex cores with a wavy displacement of the vortex center [53–55]. This instability thus can be viewed as a resonance between two normal modes of a vortex and an external strain field induced by the neighboring vortex. The Crow instability [56], on the other hand, is three-dimensional, in which perturbations displace the vortices locally as a whole without any change in their core structure; the observed wavelengths are large compared to the core radius. This instability can be observed in aircraft tip vortices [57].

A rough estimate of the features of these instabilities, if present, can be obtained by considering the characteristic length scales in the vortex pair, namely the core radius δ and the inter-vortical separation b; their ratio, δ/b, indicates the relative

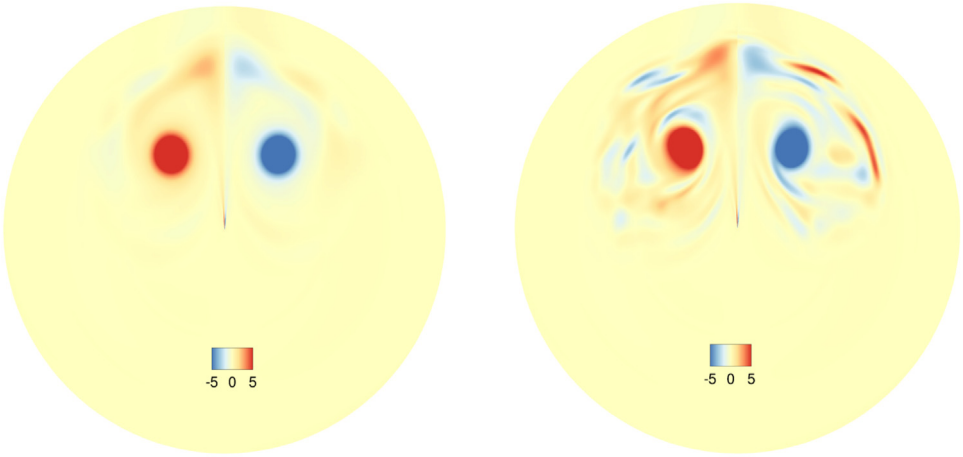

(a) Mean (b) Instantaneous

Fig. 6. Crossflow vortex field at $X/L = 2.0$ for the mean flow (a) and a representative instantaneous flow (b) shown using ω_z.

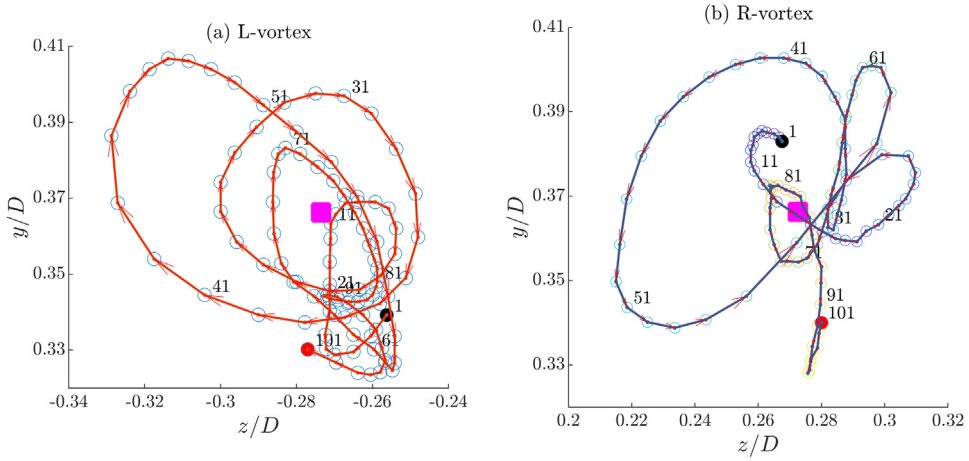

Fig. 7. Phase-portrait of instantaneous vortices at $X/L = 2.0$. The location of the mean vortex is shown as the large filled square. Black and red circles respectively indicate the beginning and end of the trajectory. (For interpretation of the references to color in this figure legend, the reader is referred to the web version of this article.)

distance between the vortices. As discussed earlier, for the current flow the value of ratio δ/b is about 0.18. This value lies in the range [0.1 1.2] that can trigger both long and short wave instabilities [58], though Reynolds number considerations are also important, which will be considered in the subsequent analysis.

The instabilities existing in the flowfield are now investigated in detail through both temporal and spatial stability analyses of the representative streamwise vortex pair. The possibility of a global mode is not examined in the current work but pursued in a separate study [59] albeit at a lower *Re*. Leweke and Williamson [60] have argued that three-dimensional instabilities in the wake could be linked to general 2D stability mechanisms such as elliptic instability. Parallel flow is assumed in the streamwise direction; this is a reasonable assumption since the streamwise variation of the mean flow is relatively small at distances sufficiently downstream of the body such as those considered here. As such, stability characteristics of the vortices predicted with parallel flow assumption provide a reasonable description of the meandering phenomena [15].

4.1. Basic state

The mean afterbody vortex pair at $X/L = 2.0$ as discussed earlier is considered for the stability analysis and the basic state is obtained by mapping this flow to an equivalent theoretical vortex model. The fitting of an afterbody vortex to a known theoretical model enables the examination of pure vortex without any numerical noise while retaining essential properties, and also allows comparisons with other physical vortices investigated in the literature. Further, a fitted model vortex offers the flexibility to extend the domain arbitrarily without compromising effects due to boundaries. García-Ortiz et al. [13] have argued that in wingtip vortices, the use of classical vortex models allows generalization to a set of theoretical parameters and thus can be useful for comparing different passive and active control strategies.

Afterbody vortices, such as the ones of interest, are characterized by two components: swirl and strain. While the swirl effect is accounted through the radially varying in-plane velocity field, the axial velocity provides the strain field [61]. The vortical field at location $X/L = 2.0$ was shown earlier in Fig. 6, while the axial velocity distribution in the vortex is shown in Fig. 9(a). As expected, the velocity is minimum at the center of the vortex and increases along the radial direction, eventually reaching free-stream values about 10 core radii (δ) away from the center. The quantitative profiles in Fig. 9(b) at different vertical locations show typical wake-like behavior. The relatively close proximity results in the observation that the magnitude of $\bar{u}$ between the

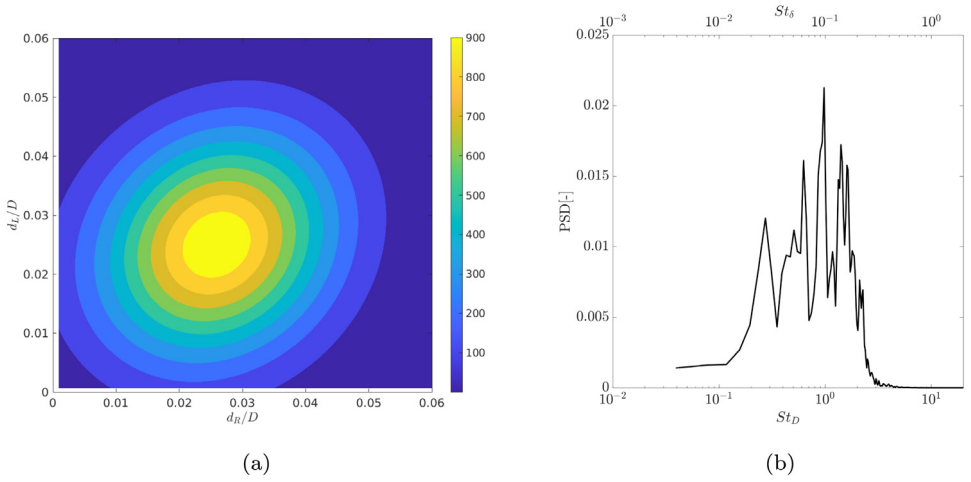

Fig. 8. Characterization of streamwise vortex pair at $X/L = 2.0$. (a) Gaussian joint PDF of instantaneous vortices. (b) Spectral content in vortex core fluctuations using Welch PSD for the **R**-vortex. Non-dimensional frequencies are shown based on the cylinder diameter, $St_D = U_\infty D/\nu$ as well as vortex core diameter, $St_\delta = U_\infty \delta/\nu$.

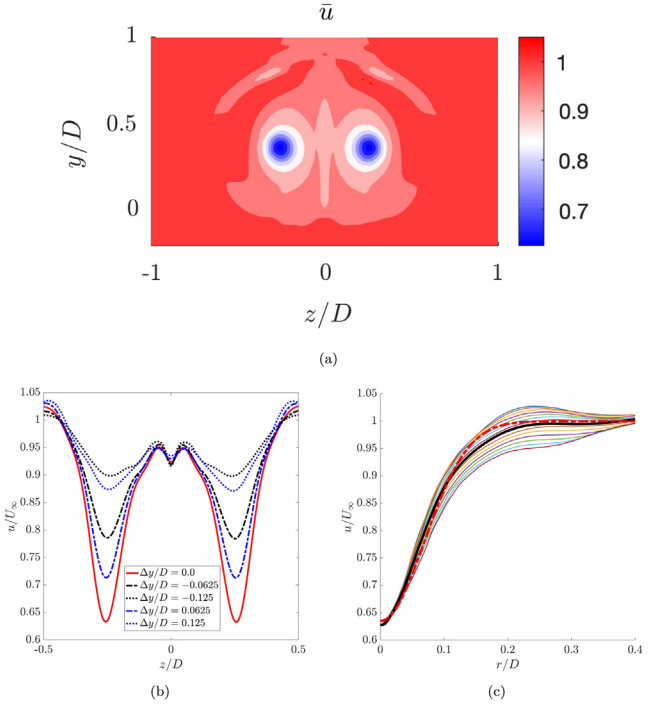

Fig. 9. Axial velocity distribution at a streamwise location $X/L = 2.0$. (a) $\bar{u}$ contours. (b) Wake-like behavior shown by velocity distributions at different vertical locations measured from the vortex center. (c) Fitting of axial velocity from simulations to the Batchelor vortex. The thick black line indicates the azimuthally averaged axial velocity, and the red dashed line indicates the axial velocity in the fitted Batchelor vortex. Note the vortex in the simulation is recentered at (0,0) after interpolating to the cylindrical coordinate system. (For interpretation of the references to color in this figure legend, the reader is referred to the web version of this article.)

vortices is lower than the free-stream flow velocity. This motivates the use of a vortex pair as opposed to an isolated **L** or **R** vortex for the present analysis.

Wake vortices have been modeled with different theoretical models that contain their characteristic information. Vortex models used in the literature for analyses of wingtip or similar vortices include the Batchelor or q-vortex [9], Lamb–Oseen vortex [62], Lamb–Chaplygin vortex [63], Rankine vortex [64] and Moore–Saffman vortex model [65]. Among these, the Batchelor and Moore–Saffman models account for axial flow and hence are more realistic in providing the dynamics of interest in this work.

We employ the Batchelor model to match the individual vortices in the current streamwise vortex pair as the role of the axial velocity in the stability mechanism may be crucial. Although this model vortex is typically expressed in cylindrical coordinates, we analyze them in the Cartesian system to account for the two vortices in the pair. In this system, the velocity components for the Batchelor vortex can be written as [25]:

$$u = 1 - \gamma(x)\exp\left(\frac{-r^2}{\delta(x)^2}\right) \tag{7a}$$

$$v = -\frac{\kappa}{r^2}(z - z_0)\left(1 - \exp\left(\frac{-r^2}{\delta(x)^2}\right)\right) \tag{7b}$$

$$w = \frac{\kappa}{r^2}(y - y_0)\left(1 - \exp\left(\frac{-r^2}{\delta(x)^2}\right)\right) \tag{7c}$$

where (y_0, z_0) is the center of the vortex and $r^2 = (y-y_0)^2 + (z-z_0)^2$. The quantity $\delta(x)$ corresponds physically to the dimensionless local vortex core radius. $\gamma(x)$ is the axial velocity defect and κ is a swirl strength parameter.

For the current analysis, one vortex is first matched to the model, and the other anti-symmetric vortex is then placed at the separation distance b. The simulation results are first interpolated on a cylindrical grid and the axial velocity u is then azimuthally averaged to obtain the parameters for the fitted Batchelor vortex. Edstrand et al. [9] have found that stability results are insensitive to the averaging process. Fig. 9(c) shows the radial variation of axial velocity at different azimuthal locations. The azimuthally averaged vortex velocity, as well as the fitted Batchelor vortex model, are also shown.

Fig. 10 compares the velocity fields in mean **R**-vortex obtained directly from simulations with those of the fitted vortex used for stability analysis. All the three velocity components considered in the model show good match with the LES data. The parameters of this matched Batchelor vortex are $\delta = 0.0972$, $\gamma = 0.365$, $\kappa = 0.07$, to obtain a non-dimensional swirl parameter $q = \kappa/(\delta\gamma) = 1.9731$. This value of q is much smaller than the $q = 4.41$ obtained for trailing edge vortex in [9]. The present parameters correspond to a Reynolds number based on the core radius as $Re_\delta \equiv U_\infty \delta/\nu \simeq 2500$, which is much lower compared to $Re_\delta = 27{,}200$ used in the stability study of wingtip vortices [9].

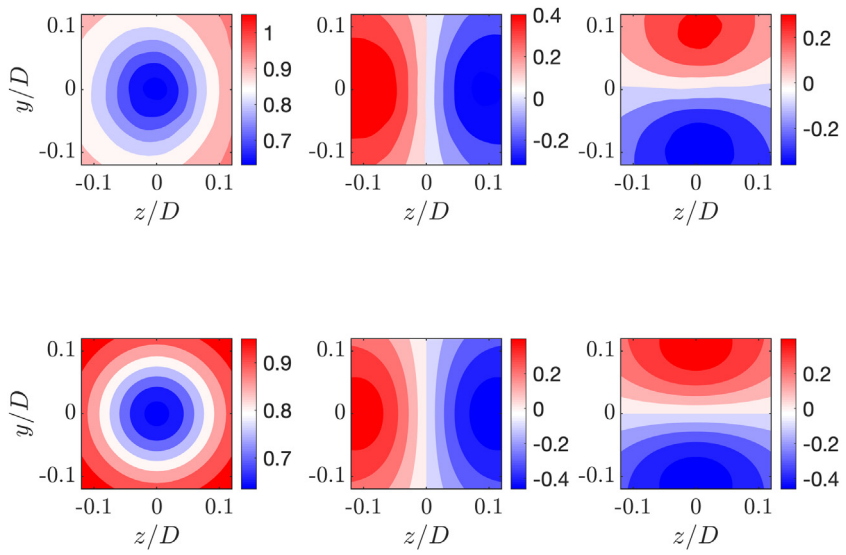

Fig. 10. Top: **R**-vortex from the simulation. Bottom: Theoretical Model (Batchelor vortex). U, V, W velocity components are shown from left to right. Note the **R**-vortex in simulation is centered to (0,0) to compare with the fitted Batchelor vortex.

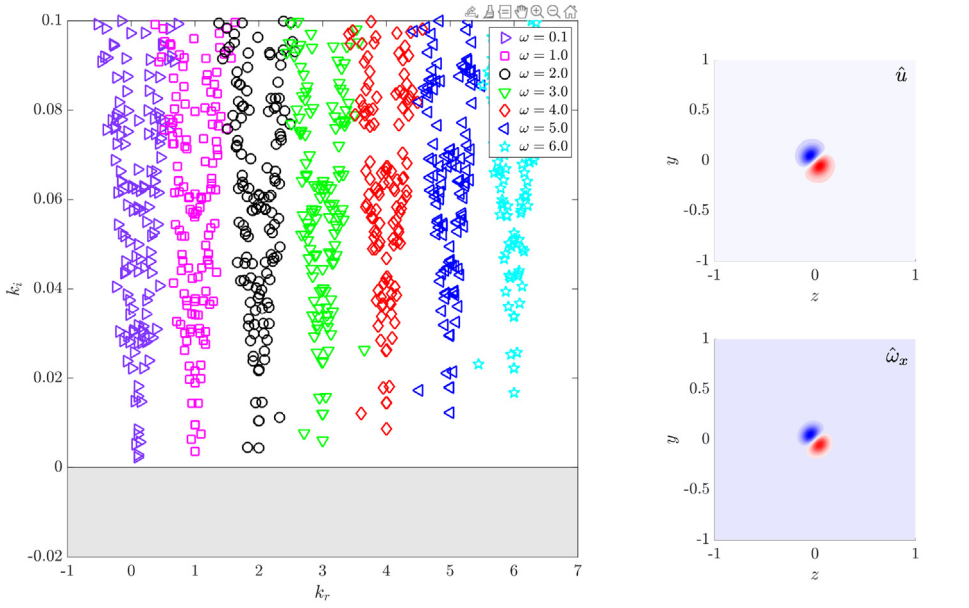

(a) Spatial analysis for $\omega \in [0.1\ 6.0]$.

(b) Least stable mode at $\omega = 1$ ($k = 0.9346 + 0.0025i$).

Fig. 11. Eigenspectrum from spatial analyses of an isolated vortex for a range of frequencies (a). Shaded portion indicates the region of growing modes ($k_i < 0$). The least stable mode at $\omega = 1$ shows $m = 1$ elliptic instability (b).

4.2. Stability mechanism

Now we present the results from linear stability analysis. Consistent with the simulations, a spanwise coordinate system is used in which two inhomogeneous spatial directions, y and z, are resolved simultaneously, while the axial direction, x, is considered to be locally homogeneous.

Before showing the dynamics of the vortex pair, we first discuss the stability characteristics of an isolated vortex. Fig. 11(a) shows results from spatial analyses of this vortex for input frequency varying from $\omega = 0.1$ to $\omega = 6.0$. A 60×60 grid on a domain of $y_\infty, z_\infty \approx 20\delta$ with stretching factor $c = 0.975$ is used for these analyses. As seen from the figure, the vortex is stable for the entire frequency range $\omega \in [0.1\ 6.0]$. The vortex becomes increasingly more stable as the frequency is increased. For the lowest input frequency $\omega = 0.1$, the least stable mode is obtained at $k \equiv k_r + ik_i = 0.0992 + 0.0023i$; the positive value of k_i in the spatial analysis indicates a decaying mode (see Appendix). The spatial structure of a representative mode at $\omega = 1$ is shown in Fig. 11(b). Both the axial velocity and vorticity fluctuations show dipole structures indicating the $|m| = 1$ elliptic mode; this mode is typically observed to be the dominant instability mechanism in wake vortices [1,9].

Now we consider the change in stability characteristics due to the presence of a counter-rotating vortex next to the above stable vortex. Based on the LES data, the counter-rotating mean vortex centers are separated by $b/\delta = 5.6132$. This relatively large separation between the vortices increases the computational requirement enormously because the stretching parameter needs to be relaxed to as low as 0.75, with a corresponding increase

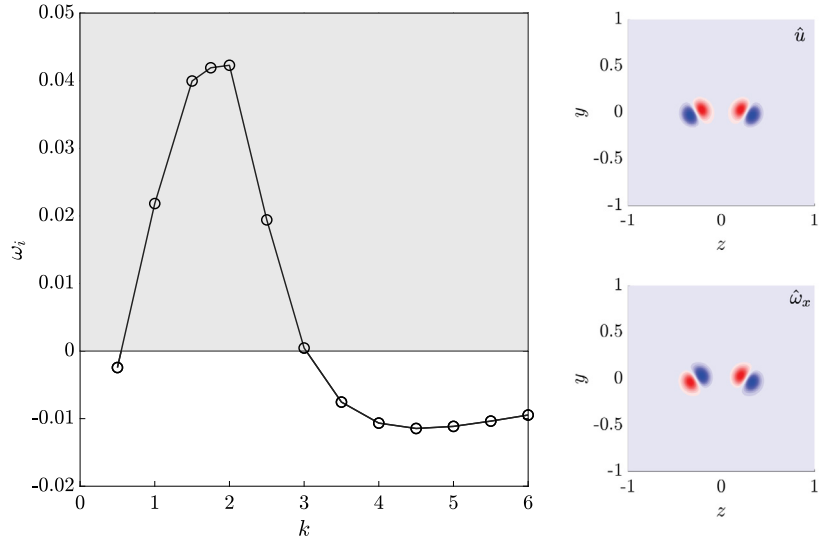

(a) Temporal analysis for $k \in [0.0\ 6.0]$.

(b) Unstable mode at $k = 2$.

Fig. 12. Eigenspectra from temporal analyses of the vortex pair for a range of wavenumbers (a). Shaded portion indicates the region of growing modes ($\omega_i > 0$). Structure of the fastest growing mode at all wavenumbers is shown in (b).

in the grid size to ensure sufficient accuracy. The parallel spatial analysis, performed above for the isolated vortex, is natural for the study of the vortex pair also, since it directly provides the wavenumber at which the flow can become unstable. However, since the grid size required for vortex pair is significantly larger (up to 150 × 150) than that for an isolated vortex, the computational burden is eased by first performing temporal stability analyses for a given wavenumber range, while spatial analysis at the most unstable frequency is later employed to further ensure the accuracy of results.

The temporal analysis results for a streamwise wavenumber sweep of $k \in [0.5\ \ 6.0]$ are shown in Fig. 12(a). These results are obtained by using a 140 × 140 Cheb-tanh grid that gives a dense matrix of 78,400 × 78,400. The vortex pair displays unstable eigenmodes at wavenumbers $1.0 \leq k \leq 3.0$, with growth rate increasing between $k = 1.0$ and $k = 2.0$. As the input wavenumber increases beyond $k = 2.0$, the modes become less unstable and only stable modes are recovered for $k > 3.0$. For the subsequent analyses, we focus on the wavenumber $k = 2.0$ at which the fastest growing modes are recovered. Fig. 13(a) shows the convergence of dominant modes in the eigenspectrum at this wavenumber as obtained by performing the analysis on a finer 150 × 150 grid. Both grids recover most unstable modes at $\omega \equiv \omega_r + i\omega_i = \pm 1.988 + 0.0417i$ (note only the positive frequency ω_r mode is shown). The phase speed of this mode is $c_r \equiv \omega_r/k = 0.9940$.

In order to confirm that spatial analysis also recovers similar instabilities, we show the eigenspectrum from this approach at input frequency $\omega = 2.0$ in Fig. 13(b). Note that the matrix size for the spatial problem is very large (137,200 × 137,200) for a similar grid size of 140 × 140 and solving this eigenvalue problem with a Krylov size of 100, requires about 100 gigabytes of the physical system memory. The spatial analysis recovers an unstable mode at $k \equiv k_r + ik_i = \pm 2.0138 - 0.0473i$ as shown in the unstable region ($k_i < 0$) in Fig. 13(b). The phase speed of this mode, $c_r \equiv \omega/k_r = 0.9932$, is very similar to that obtained from the temporal analysis earlier. The recovery of analogous instabilities in both spatial and temporal approaches further validates present observations.

The structure of this mode as obtained from both temporal and spatial approaches is very similar as shown in Fig. 12(b). The shape again exhibits a dipole form representing the $|m| = 1$ elliptic mode for both vortices in the pair. This dipole is extracted in both the axial velocity and vorticity fluctuations, but it is symmetric about the mid-plane ($z = 0$) in the former, but anti-symmetric in the latter. This is consistent with the symmetry of the mean flow. The inclination of the dipole with respect to the horizontal axis is about 30°.

The frequency of the most unstable mode as obtained from the temporal analysis is $\omega \simeq 1.988$, or equivalently $St_D \simeq 0.32$. This low-frequency was observed in the vortex flowfield through spectral analysis (Fig. 8(b))). In the experimental work of Zigunov et al. [27], this low-frequency was observed and was conjectured to be related to fluctuations due to interactions of cores. The present stability analysis confirms this hypothesis and establishes meandering as a low-frequency phenomenon in afterbody flows in similarity with vortices in aircraft wakes [52]. The linear receptivity analysis of Bölle et al. [12] indicates the presence of a frequency-dependent non-normal mechanism, which enables a description in terms of freestream disturbance forcing and vortex core response. A crucial finding relevant to the energetic dynamics is the relative lack of dependence on freestream intensity on the frequency response.

To further confirm the role of the interaction between the vortices as a necessary mechanism for the recovery of unstable modes, we perform the temporal stability analysis for an isolated vortex with the same swirl and strain as in each individual vortex in the pair. Fig. 14(a) shows the result from this analysis along with grid convergence for the dominant modes as obtained with two grids. Unlike in the two-vortex system, all modes recovered in this analysis are decaying. The least stable modes are found at $\omega = \pm 2.0001 - 0.0047i$ exhibiting dipole structures for both vorticity and axial velocity, which is similar to that shown in Fig. 11(b).

The external strain field is influenced by the neighboring vortex, and is accounted for in the stability calculations through the axial velocity component. The correlation analysis of Section 3.2, based on the phenomenological description of instantaneous vortex cores on a sectional plane, indicates only weak influence of the vortices on one another. That analysis, however, did not include the axial velocity component, whose role in destabilizing the vortices is now clarified. A stable vortex can become unstable even without the presence of axial flow (as in the Kelvin vortex) due to an elliptic instability of the core; however, the

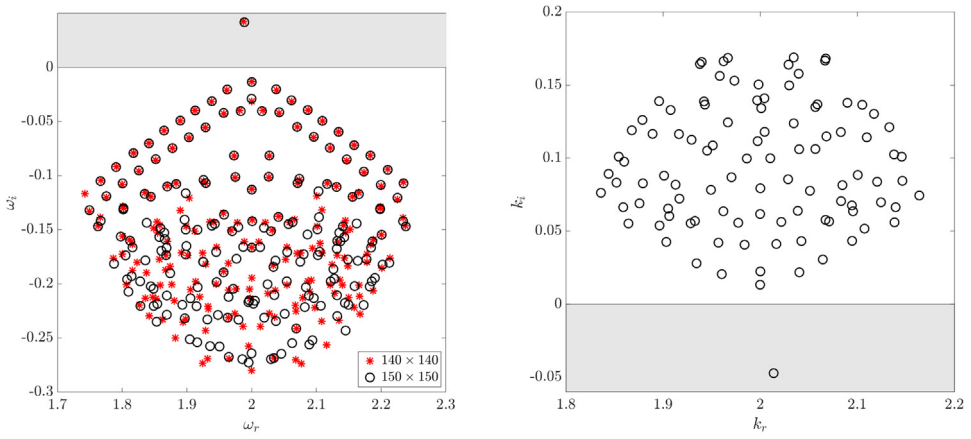

(a) Temporal ($k = 2$). (b) Spatial ($\omega = 2$).

Fig. 13. Eigenspectra from temporal (a) and spatial (b) analyses of the afterbody vortex pair. Both approaches show analogous instabilities at a phase speed of about 0.99.

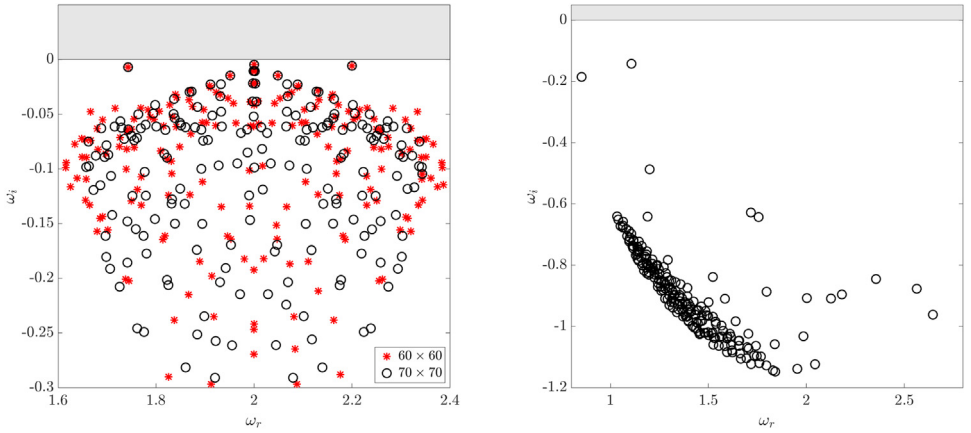

(a) Isolated vortex. (b) Vortex pair ($u = 0$).

Fig. 14. Eigenspectra from temporal analysis at $k = 2.0$. (a) Isolated vortex with axial velocity. (b) Vortex pair with no axial velocity.

presence of an axial flow can make an otherwise stable vortex unstable [64,66]. In order to examine the effects of this strain, the temporal stability analysis was repeated on the afterbody vortex pair by setting the axial velocity to zero. The problem then becomes essentially similar to Rankine vortex models used in the literature to study elliptic instabilities [16]. The eigenspectrum thus obtained is shown in Fig. 14(b). A key observation is that unlike the analysis with the axial velocity (Fig. 13(a)), no unstable mode is recovered in this calculation. Further, the modes are far removed from the zero axis. Although not shown, the shapes of dominant modes continue to show helical structures. The present analysis thus shows that it is necessary to consider a vortex model that includes the strain field in order to recover the correct instability behavior in afterbody vortices.

Finally, the possible presence of long-wavelength (small k) Crow instability in the flow is investigated. The least stable mode at $k = 2$ in Fig. 12(b) is inclined at 30° to the horizontal. The Crow instability on the other hand typically manifests a 45° inclination in the structure [67]. To confirm this further at low wavenumbers, the temporal analysis was performed using a k-parameter sweep between 0.0 and 1.0 at increments of 0.1. Fig. 15 shows the resulting eigenspectra for all these wavenumbers for the current vortex pair. No unstable mode is observed in the k-range of [0.0 0.4], and the first unstable mode occurs at $k = 0.5$. The growth rate of modes continues to increase with wavenumber until $k = 2.0$ as discussed earlier. This indicates the absence of the Crow instability in this flow, although simulations with a longer domain may be necessary to establish this fact numerically. Further, the flow conditions that lead to a change in the non-dimensional swirl parameter or the Reynolds number may affect this observation, as discussed in [23]. Another key parameter in the analysis that determines the interaction between the two vortices is the separation distance, b/δ. As stated earlier, if this distance varies substantially with the upsweep angle ϕ of the afterbody, the analysis needs to be repeated to examine the stability mechanism.

5. Conclusions

High fidelity simulations are employed to examine the instability dynamics of a pair of relatively closely spaced streamwise vortices arising from a flat upswept basal surface. Such vortices arise in various three-dimensional scenarios such as Ahmed bodies, cars and trains. In this study, a simulated cargo aircraft fuselage aft section with a representative 20° basal upsweep is considered because of its implication on cargo drops and downstream aircraft. The primary feature, a horseshoe-shaped structure, develops around the periphery of the base and ultimately lifts away from the surface to manifest a three-dimensional, generally streamwise-oriented, vortex pair. Large Eddy Simulations

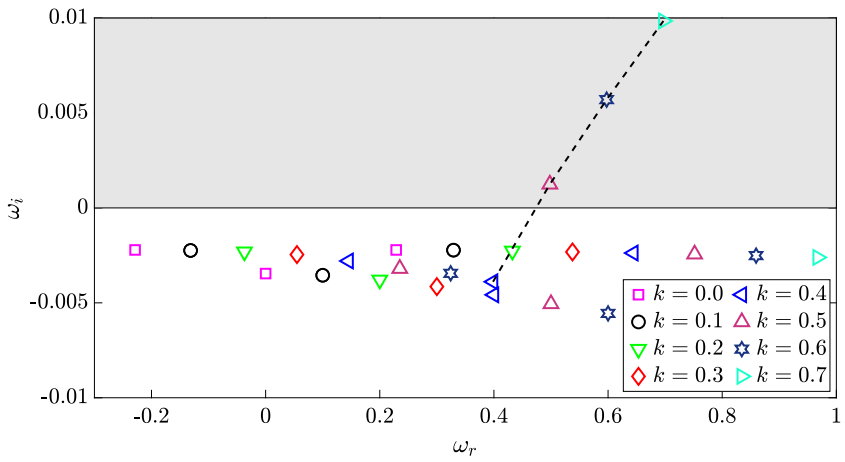

Fig. 15. Eigenspectra from temporal analyses of the afterbody vortex pair at low wavenumbers. No unstable modes are recovered below $k = 0.5$.

show that beyond the region directly influenced by the basal surface, the wake vortices are generally axisymmetric in the mean sense and exhibit low-frequency meandering in space and time. This motion is characterized by seemingly random displacement of the vortex cores, although the time trajectory of the displacement of the core shows a rotation sense commensurate with the swirl in the vortices. The instability mechanism underlying meandering is analyzed using a linear stability approach on the time-averaged streamwise vortex pair. The mean vortex obtained from the simulations is first matched to a suitable Batchelor vortex; a counter-rotating model vortex is then placed at an appropriate separation distance, derived from the LES, from the first vortex. Both spatial and temporal analyses confirm the presence of an elliptic instability with the structures of the unstable modes being similar to $|m| = 1$ modes. For an isolated vortex, these modes are found to be stable. Swirl and strain effects are also delineated for the vortex pair, and for the current conditions, the effect of compressibility is shown to be minimal at low Mach number of $M = 0.1$. The unstable modes are obtained at relatively low frequency with the presence of axial velocity as primary mechanism for instability; connections to literature on resolvent-based analyses of the influence of freestream disturbances are noted. On the other hand, the long-wavelength Crow instability is found to be absent for this vortex pair at the separation distance dictated by the geometry and flow parameters in this study.

Declaration of competing interest

The authors declare that they have no known competing financial interests or personal relationships that could have appeared to influence the work reported in this paper.

Acknowledgments

This material is based upon work supported by the Air Force Office of Scientific Research, USA under award number FA9550-17-1-0228 (monitor: Gregg Abate). DVG acknowledges partial support from the Collaborative Center for Aeronautical Sciences (FA8650-19-2-2204). The authors thank F. Alvi, F. Zigunov, and P. Sellappan for several fruitful communications. Simulations were carried out using resources provided by the U.S. Department of Defense High-Performance Computing Modernization Program and the Ohio Supercomputer Center.

Appendix. Linear stability equations

Linear stability equations are obtained by substituting the modal form of the perturbations (4) in the linearized Navier–Stokes equations (3),

$$\left(\underbrace{\begin{bmatrix} \mathcal{L} & \overline{U}_y & \overline{U}_z & 0 \\ 0 & \mathcal{L}+\overline{V}_y & \overline{V}_z & D_y \\ 0 & \overline{W}_y & \mathcal{L}+\overline{W}_z & D_z \\ 0 & D_y & D_z & 0 \end{bmatrix}}_{\mathbb{A}_0} + k \underbrace{\begin{bmatrix} i\overline{U} & 0 & 0 & i \\ 0 & i\overline{U} & 0 & 0 \\ 0 & 0 & i\overline{U} & 0 \\ i & 0 & 0 & 0 \end{bmatrix}}_{\mathbb{A}_1} + k^2 \underbrace{\begin{bmatrix} IRe^{-1} & 0 & 0 & 0 \\ 0 & IRe^{-1} & 0 & 0 \\ 0 & 0 & IRe^{-1} & 0 \\ 0 & 0 & 0 & 0 \end{bmatrix}}_{\mathbb{A}_2} - \omega \underbrace{\begin{bmatrix} i & 0 & 0 & 0 \\ 0 & i & 0 & 0 \\ 0 & 0 & i & 0 \\ 0 & 0 & 0 & 0 \end{bmatrix}}_{\mathbb{B}} \right) \begin{bmatrix} \tilde{u} \\ \tilde{v} \\ \tilde{w} \\ \tilde{p} \end{bmatrix} = 0$$

where

$$\mathcal{L} = \overline{V} D_y + \overline{W} D_z - \frac{D_{yy} + D_{zz}}{Re}. \tag{A.1}$$

D_y, D_{yy} etc. represent first and second-order differentiation matrices. I is the identity matrix.

For the temporal analysis, the real wavenumber k is specified, while $\omega = \omega_r + i\omega_i$ is a complex quantity denoting the circular frequency, ω_r, and growth rate, ω_i. The generalized eigenvalue problem, following Eqs. (A.1), is then:

$$\mathbb{A}\tilde{\boldsymbol{q}} = \omega \mathbb{B} \tilde{\boldsymbol{q}}. \tag{A.2}$$

with $\tilde{\boldsymbol{q}} = \{\tilde{u}, \tilde{v}, \tilde{w}, \tilde{p}\}^T$ and $\mathbb{A} = \mathbb{A}_0 + k\mathbb{A}_1 + k^2\mathbb{A}_2$.

For spatial stability analysis, the streamwise wavenumber $k = k_r + ik_i$ represents the complex eigenvalue, with $k_i < 0$ indicating spatial exponential growth, and ω is a real specified circular frequency. In this case, Eqs. (A.1) present a quadratic eigenvalue problem:

$$(\mathbb{A}_0' + k\mathbb{A}_1 + k^2\mathbb{A}_2)\tilde{\boldsymbol{q}} = 0 \tag{A.3}$$

with $\mathbb{A}_0' = \mathbb{A}_0 - \omega\mathbb{B}$.

Although the problem can be solved directly, the quadratic eigenvalue problem can become very expensive for large matrices. Therefore, it is converted into a linear eigenvalue problem by using the companion matrix technique [68]. The matrix size of this spatial eigenvalue problem is therefore 75% higher than the temporal approach due to the padding of three auxiliary variables at every grid point.

References

[1] C. Del Pino, J. Lopez-Alonso, L. Parras, R. Fernandez-Feria, Dynamics of the wing-tip vortex in the near field of a NACA 0012 aerofoil, Aeronaut. J. 115 (1166) (2011) 229–239.
[2] B.-F. Ma, Z. Wang, I. Gursul, Symmetry breaking and instabilities of conical vortex pairs over slender delta wings, J. Fluid Mech. 832 (2017) 41–72.
[3] D. Bulathsinghala, R. Jackson, Z. Wang, I. Gursul, Afterbody vortices of axisymmetric cylinders with a slanted base, Exp. Fluids 58 (5) (2017) 60.
[4] V. Corsiglia, R. Schwind, N. Chigier, Rapid scanning, three-dimensional hot-wire AnemometerSurveys of wing-tip vortices, J. Aircr. 10 (12) (1973) 752–757.
[5] G. Baker, S. Barker, K. Bofah, P. Saffman, Laser anemometer measurements of trailing vortices in water, J. Fluid Mech. 65 (2) (1974) 325–336.
[6] W.J. Devenport, M.C. Rife, S.I. Liapis, G.J. Follin, The structure and development of a wing-tip vortex, J. Fluid Mech. 312 (1996) 67–106.
[7] S.J. Beresh, J.F. Henfling, R.W. Spillers, Meander of a fin trailing vortex and the origin of its turbulence, Exp. Fluids 49 (3) (2010) 599–611.
[8] J. Feys, S.A. Maslowe, Linear stability of the moore-saffman model for a trailing wingtip vortex, Phys. Fluids 26 (2) (2014) 024108.
[9] A.M. Edstrand, T.B. Davis, P.J. Schmid, K. Taira, L.N. Cattafesta, On the mechanism of trailing vortex wandering, J. Fluid Mech. 801 (2016).
[10] Y. Xiang, Z.-P. Cheng, Y.-M. Wu, H. Liu, F. Wang, Scaling analysis on the dynamic and instability characteristics of isolated wingtip vortex, AIAA J. 59 (12) (2021) 5198–5210.
[11] S. Qiu, Z. Cheng, H. Xu, Y. Xiang, H. Liu, On the characteristics and mechanism of perturbation modes with asymptotic growth in trailing vortices, J. Fluid Mech. 918 (2021).
[12] T. Bölle, V. Brion, J.-C. Robinet, D. Sipp, L. Jacquin, On the linear receptivity of trailing vortices, J. Fluid Mech. 908 (2021).
[13] J.H. García-Ortiz, F.J. Blanco-Rodríguez, L. Parras, C. Del Pino, Experimental observations of the effects of spanwise blowing on the wingtip vortex evolution at low Reynolds numbers, Eur. J. Mech. B Fluids 80 (2020) 133–145.
[14] L. Parras, R. Fernandez-Feria, Spatial stability and the onset of absolute instability of batchelor's vortex for high swirl numbers, J. Fluid Mech. 583 (2007) 27–43.
[15] A.M. Edstrand, P.J. Schmid, K. Taira, L.N. Cattafesta, A parallel stability analysis of a trailing vortex wake, J. Fluid Mech. 837 (2018) 858–895.
[16] R.R. Kerswell, Elliptical instability, Annu. Rev. Fluid Mech. 34 (1) (2002) 83–113.
[17] Z.-P. Cheng, S.-Y. Qiu, Y. Xiang, H. Liu, Quantitative features of wingtip vortex wandering based on the linear stability analysis, AIAA J. (2019) 2694–2709.
[18] Navrose, V. Brion, L. Jacquin, Transient growth in the near wake region of the flow past a finite span wing, J. Fluid Mech. 866 (2019) 399–430.
[19] T. Morel, The effect of base slant on the flow pattern and drag of three-dimensional bodies with blunt ends, in: Aerodynamic Drag Mechanisms of Bluff Bodies and Road Vehicles, Springer, 1978, pp. 191–226.
[20] H. Lienhart, C. Stoots, S. Becker, Flow and turbulence structures in the wake of a simplified car model (ahmed modell), in: New Results in Numerical and Experimental Fluid Mechanics III, Springer, 2002, pp. 323–330.
[21] G. Rossitto, C. Sicot, V. Ferrand, J. Borée, F. Harambat, Influence of afterbody rounding on the pressure distribution over a fastback vehicle, Exp. Fluids 57 (3) (2016) 43.
[22] J. Bell, D. Burton, M. Thompson, A. Herbst, J. Sheridan, Dynamics of trailing vortices in the wake of a generic high-speed train, J. Fluids Struct. 65 (2016) 238–256.
[23] S. Hein, V. Theofilis, On instability characteristics of isolated vortices and models of trailing-vortex systems, Comput. & Fluids 33 (5–6) (2004) 741–753.
[24] L.M. González, R. Gómez-Blanco, V. Theofilis, Eigenmodes of a counter-rotating vortex dipole, AIAA J. 46 (11) (2008) 2796–2805.
[25] P. Paredes, V. Theofilis, D. Rodriguez, J. Tendero, The PSE-3D instability analysis methodology for flows depending strongly on two and weakly on the third spatial dimension, in: 6th AIAA Theoretical Fluid Mechanics Conference, 2011, p. 3752.
[26] F. Zigunov, P. Sellappan, F. Alvi, Reynolds number and slant angle effects on the flow over a slanted cylinder afterbody, J. Fluid Mech. 893 (2020).
[27] F. Zigunov, P. Sellappan, F.S. Alvi, Dynamics of the slanted cylinder afterbody vortices, in: AIAA Scitech 2020 Forum, 2020, p. 1322.
[28] D.J. Garmann, M.R. Visbal, High-fidelity simulations of afterbody vortex flows, AIAA J. 57 (9) (2019) 3980–3990, http://dx.doi.org/10.2514/1.J058284.
[29] R. Ranjan, M. Aultman, D. Gaitonde, Mean flowfield evolution with upsweep angle in a simulated cargo fuselage aftbody, J. Aircr. 57 (6) (2020) 1156–1169.
[30] D. Bulathsinghala, Z. Wang, I. Gursul, Modified near-wakes of axisymmetric cylinders with slanted base, Aerosp. Sci. Technol. (2019).
[31] R. Jackson, Z. Wang, I. Gursul, Control of upswept afterbody vortices using continuous and pulsed blowing, J. Aircr. 57 (1) (2020) 76–92, http://dx.doi.org/10.2514/1.C035639.
[32] F.N. Holzäpfel, L. Strauss, C.W. Schwarz, Assessment of dynamic pairwise wake vortex separations for approach and landing at vienna airport, in: AIAA Aviation 2019 Forum, 2019, p. 3178.
[33] R.J. Epstein, M.C. Carbonaro, F. Caudron, Experimental investigation of the flowfield about an unswept afterbody, J. Aircr. 31 (6) (1994) 1281–1290.
[34] Y. Bury, T. Jardin, A. Klöckner, Experimental investigation of the vortical activity in the close wake of a simplified military transport aircraft, Exp. Fluids 54 (5) (2013) 1524.
[35] J. Mathew, R. Lechner, H. Foysi, J. Sesterhenn, R. Friedrich, An explicit filtering method for large eddy simulation of compressible flows, Phys. Fluids 15 (8) (2003) 2279–2289.
[36] R.M. Beam, R.F. Warming, An implicit finite-difference algorithm for hyperbolic systems in conservation-law form, J. Comput. Phys. 22 (1) (1976) 87–110.
[37] T.H. Pulliam, D. Chaussee, A diagonal form of an implicit approximate-factorization algorithm, J. Comput. Phys. 39 (2) (1981) 347–363.
[38] D.V. Gaitonde, M.R. Visbal, High-order Schemes for Navier-Stokes Equations: Algorithm and Implementation into FDL3DI, Technical Report, Air Force Research Lab Wright-Patterson AFB OH Air Vehicles Directorate, 1998.
[39] M.R. Visbal, D.V. Gaitonde, On the use of higher-order finite-difference schemes on curvilinear and deforming meshes, J. Comput. Phys. 181 (1) (2002) 155–185.
[40] W.E. Arnoldi, The principle of minimized iterations in the solution of the matrix eigenvalue problem, Quart. Appl. Math. 9 (1) (1951) 17–29.
[41] R.B. Lehoucq, D.C. Sorensen, C. Yang, ARPACK Users' Guide: Solution of Large-Scale Eigenvalue Problems with Implicitly Restarted Arnoldi Methods, SIAM, 1998.
[42] P. Paredes, Advances in Global Instability Computations: from Incompressible to Hypersonic Flow (PhD Dissertation), Universidad Politécnica de Madrid, 2014.
[43] E.W. Mayer, K.G. Powell, Viscous and inviscid instabilities of a trailing vortex, J. Fluid Mech. 245 (1992) 91–114.
[44] G. Haller, An objective definition of a vortex, J. Fluid Mech. 525 (2005) 1–26.
[45] R. Ranjan, D. Gaitonde, Hysteresis in slanted-base-cylinder afterbody flows, Aerosp. Sci. Technol. 106 (2020) 106138.
[46] R. Ranjan, J.-C. Robinet, D.V. Gaitonde, Meandering of longitudinal wake vortices in slanted base afterbody flows, in: AIAA Scitech 2020 Forum, 2020, p. 1532.
[47] M. Dghim, M. Ferchichi, H. Fellouah, On the effect of active flow control on the meandering of a wing-tip vortex, J. Fluid Mech. 896 (2020) A30.
[48] L. Graftieaux, M. Michard, N. Grosjean, Combining PIV, POD and vortex identification algorithms for the study of unsteady turbulent swirling flows, Meas. Sci. Technol. 12 (9) (2001) 1422.
[49] S. Green, A. Acosta, Unsteady flow in trailing vortices, J. Fluid Mech. 227 (1991) 107–134.
[50] R.E. Gordnier, M.R. Visbal, Compact difference scheme applied to simulation of low-Sweep Delta wing flow, AIAA J. 43 (8) (2005) 1744–1752.
[51] R.W. Jackson, Z. Wang, I. Gursul, Control of afterbody vortices by blowing, in: 45th AIAA Fluid Dynamics Conference, 2015, p. 2777.
[52] L. Jacquin, D. Fabre, P. Geffroy, E. Coustols, The properties of a transport aircraft wake in the extended near field-an experimental study, in: 39th Aerospace Sciences Meeting and Exhibit, 2001, p. 1038.
[53] S. Widnall, D. Bliss, A. Zalay, Theoretical and experimental study of the stability of a vortex pair, in: Aircraft Wake Turbulence and Its Detection, Springer, 1971, pp. 305–338.
[54] C.-Y. Tsai, S.E. Widnall, The stability of short waves on a straight vortex filament in a weak externally imposed strain field, J. Fluid Mech. 73 (4) (1976) 721–733.
[55] D. Sipp, L. Jacquin, Widnall instabilities in vortex pairs, Phys. Fluids 15 (7) (2003) 1861–1874.
[56] S.C. Crow, Stability theory for a pair of trailing vortices, AIAA J. 8 (12) (1970) 2172–2179.
[57] T. Leweke, C.H. Williamson, Cooperative elliptic instability of a vortex pair, J. Fluid Mech. 360 (1998) 85–119.
[58] T. Leweke, S. Le Dizes, C.H. Williamson, Dynamics and instabilities of vortex pairs, Annu. Rev. Fluid Mech. 48 (2016) 507–541.
[59] Q. Liu, D.V. Gaitonde, R. Ranjan, Global stability analysis of flow behind an upswept aftbody, AIAA J. (2021) 1–5.

[60] T. Leweke, C.H. Williamson, Three-dimensional instabilities in wake transition, Eur. J. Mech. B Fluids 17 (4) (1998) 571–586.
[61] H. Koizumi, Y. Hattori, Structures of wing-tip vortices at low Reynolds numbers and their modelling, Fluid Dyn. Res. 52 (4) (2020) 045503.
[62] A. Antkowiak, P. Brancher, Transient energy growth for the Lamb–Oseen vortex, Phys. Fluids 16 (1) (2004) L1–L4.
[63] R. Jugier, J. Fontane, L. Joly, P. Brancher, Linear two-dimensional stability of a Lamb-Oseen dipole as an aircraft wake model, Phys. Rev. Fluids 5 (1) (2020) 014701.
[64] L. Lacaze, A.-L. Birbaud, S. Le Dizès, Elliptic instability in a rankine vortex with axial flow, Phys. Fluids 17 (1) (2005) 017101.
[65] J. Feys, S.A. Maslowe, Elliptical instability of the moore–saffman model for a trailing wingtip vortex, J. Fluid Mech. 803 (2016) 556–590.
[66] L. Jacquin, D. Fabre, D. Sipp, E. Coustols, Unsteadiness, instability and turbulence in trailing vortices, C. R. Phys. 6 (4–5) (2005) 399–414.
[67] V. Brion, H. Dekerret, D. Sipp, L. Jacquin, Optimal perturbation of a vortex sheet for fast destabilization of the trailing vortices, in: 38th Fluid Dynamics Conference and Exhibit, 2008, p. 4182, http://dx.doi.org/10.2514/6.2008-4182.
[68] F. Tisseur, K. Meerbergen, The quadratic eigenvalue problem, SIAM Rev. 43 (2) (2001) 235–286.